Materials Science & Engineering A 788 (2020) 139593

Contents lists available at ScienceDirect

Materials Science & Engineering A

journal homepage: http://www.elsevier.com/locate/msea

Influence of scanning strategy and parameter on microstructural feature, residual stress and performance of Sc and Zr modified Al–Mg alloy produced by selective laser melting

Han Zhang [a,b], Dongdong Gu [a,b,*], Donghua Dai [a,b], Chenglong Ma [a,b], Yuxin Li [a,b], Ruolin Peng [a], Shuhui Li [c], Gang Liu [d], Biqi Yang [d]

[a] College of Materials Science and Technology, Nanjing University of Aeronautics and Astronautics, Yudao Street 29, Nanjing, 210016, Jiangsu Province, PR China
[b] Jiangsu Provincial Engineering Laboratory for Laser Additive Manufacturing of High-Performance Metallic Components, Nanjing University of Aeronautics and Astronautics, Yudao Street 29, Nanjing, 210016, Jiangsu Province, PR China
[c] Shanghai Key Laboratory of Digital Manufacture for Thin-Walled Structures, Shanghai Jiao Tong University, 200240, Shanghai, PR China
[d] Shanghai Institute of Spacecraft Equipment, 200240, Shanghai, PR China

ARTICLE INFO

Keywords:
Selective laser melting
Additive manufacturing
Al–Mg-Sc-Zr
Scanning strategy
Residual stress
Performance

ABSTRACT

Selective laser melting (SLM), due to its track-by-track and layer by layer localized additive manufacturing process nature, has significant requirements for the optimization of laser scanning strategy and parameter. In this work, rare earth element Sc- and Zr- modified Al–Mg alloy was processed by SLM using an "island" scanning strategy with different island sizes. The influence of island size on surface quality, microstructural feature, residual stress, tensile property and corrosion resistance of SLM-processed Al–Mg-Sc-Zr alloy was systematically investigated. Experimental results indicated that the surface smoothness was enhanced as the island size decreased, but the influence of island size on microstructural development and tensile properties was not distinct. Considerably high tensile properties above 500 MPa combined with elongations of 10%–12% were generally obtained for Al–Mg-Sc-Zr specimens processed under different island sizes. Minimum residual stress was generated at a moderate island size of 2.4 mm and the residual stress increased both at a small and a large island size. A similar tendency was also observed for the corrosion resistance of SLM processed Al–Mg-Sc-Zr specimens, where a superior corrosion resistance ($i_{corr} = 6.82 \times 10^{-6}$ A cm^{-2}) was generated at the middle island size. The different temperature gradient and thermal behaviors under different island sizes contribute to the variation of surface conditions and residual stresses. The change in corrosion behaviors under different island sizes was related to the different molten pool configurations. These findings provided the knowledge of the relationship between laser scanning strategy and properties of SLM processed Al–Mg-Sc-Zr alloy, which further facilitated process optimization and engineering applications of laser additive manufacturing of high-performance Al–Mg-Sc-Zr alloy.

1. Introduction

Additive manufacturing (AM) is a rapid prototyping technology with great application potentials, which has gained worldwide interest in recent years. Selective laser melting (SLM), also called laser powder bed fusion (LPBF), is one of the developed AM technologies [1–3]. SLM fabricates complex metal components by selectively fusing successive powder layers using a high energy laser beam controlled by a computer. The advantages offered by SLM are various, including high design freedom, short processing cycle and low material wastage [4]. Until now, plenty of metal materials can be processed by SLM, such as ferroalloys, titanium alloys, aluminum alloys, nickel-base superalloys, etc. Among various alloys, SLM processed aluminum alloy is one of the most investigated projects due to its great potential in aerospace applications. State of the art in SLM processed aluminum alloys are mainly focused on 4xxx Al–Si alloys [5–7], including AlSi10Mg, AlSi12 and AlSi7Mg. These alloys have near-eutectic compositions and short solidification ranges, which facilitate the SLM processability and decrease the tendency of

* Corresponding author. College of Materials Science and Technology, Nanjing University of Aeronautics and Astronautics, Yudao Street 29, Nanjing, 210016, Jiangsu Province, PR China.
E-mail address: dongdonggu@nuaa.edu.cn (D. Gu).

https://doi.org/10.1016/j.msea.2020.139593
Received 31 December 2019; Received in revised form 2 April 2020; Accepted 15 May 2020
Available online 19 May 2020

cracks. Although these Al–Si alloys exhibit excellent SLM processibilities, the limited mechanical properties of these alloys are not suitable for structural components applications in aerospace [8].

A newly developed SLM processable high-performance aluminum alloy is Sc- and Zr- modified 5xxx Al–Mg alloy, which has attracted wide attention owing to its excellent combination of light weight and high strength [9,10]. Since the Al–Mg-Sc-Zr alloy is the latest high performance aluminum alloy applied in SLM, researches focused on it is still in its infancy. Spierings et al. [11] investigated the microstructures of SLM processed Al–Mg-Sc-Zr alloy and found fine grains along molten pool boundaries interspersed with coarser grained regions in the center of the molten pool were generated. Further analyses indicated that the bimodal grain structures related to the temperature gradients and precipitation behaviors during the SLM process. The influence of platform temperature on the microstructure and mechanical properties of SLM processed Al–Mg-Sc-Zr alloy was studied by Shi et al. [12], who revealed a higher as-fabricated strength was obtained at a higher platform temperature of 200 °C. As a heat treatable aluminum alloy, the mechanical properties of Al–Mg-Sc-Zr alloy can be significantly enhanced after heat treatment due to the precipitation of coherent Al_3(Sc,Zr) particles [13]. Li et al. [14] researched the influence of heat treatment on the microstructures and mechanical properties of Al-3.02Mg-0.2Sc-0.1Zr alloy processed by SLM, and revealed the ductility and strength trade-off can be controlled by adjusting aging parameters. Although several studies were carried out in recent years to investigate the Al–Mg-Sc-Zr alloy processed by SLM, many aspects of process optimizations are still unclear and need to be further researched.

Generally, the process optimizations of the SLM process mainly consist of two aspects, namely laser parameters and laser scan strategies. As for the laser parameters, Spierings et al. [15] and Zhang et al. [16] investigated the influence of laser scanning speeds on the densification behaviors, microstructures and mechanical properties of SLM processed Al–Mg-Sc-Zr alloy, revealing the precipitation behaviors, dislocation densities and properties were significantly affected by laser scan speeds. A large number of previous studies have shown that the laser scanning strategy also has a considerable influence on the SLM process [1,17–19]. Island scanning strategy (also called chess board scanning strategy), as one of the most commonly used laser scanning strategies, is applied to decrease thermal residual stresses by dividing each layer into several smaller islands and shortening single scanning tracks [20]. So far, a number of studies were performed to investigate the relationship between the island scanning strategy and the properties of SLM fabricated components. Thijs et al. [1] investigated the influence of island scanning strategy on the microstructures and textures of SLM processed AlSi10Mg alloy. Chen et al. [21] studied the effects of overlap rate between island borders on residual stresses for SLM processed Ti6Al4V alloy, and indicated the residual stress was reduced as overlap rate increased within a certain degree. However, studies focused on the influence of island scanning strategy on SLM processed Al–Mg-Sc-Zr alloy are absent. The appropriate parameters of the island scanning strategy for SLM processed Al–Mg-Sc-Zr alloy and its influences on the microstructures, residual stresses and mechanical properties are unclear. In addition, different island sizes indicate different lengths of scanning vectors during the SLM process. Island size, as one of the most important parameters of island scanning strategy, can significantly affect the thermal behaviors inside molten pools and resultantly residual stresses and performances [20]. Thus it is of great significance to study the influence of island size on microstructure, residual stress, properties of SLM processed Al–Mg-Sc-Zr alloy, which can facilitate its process optimizations and further engineering applications.

In this study, different island sizes varied from 1.2 mm to 7.2 mm were applied to fabricate Al–Mg-Sc-Zr specimens. The influence of island size on densification behavior, microstructure, residual stress, tensile property, and corrosion resistance were systematically investigated. The mechanisms of different properties under various island sizes were analyzed and discussed. The optimal island size for SLM processed Al–Mg-Sc-Zr alloy was further summarized and suggested in this research.

2. Experiment methods

2.1. Materials and specimen preparation

Gas-atomized Al-4.2Mg-0.4Sc-0.2Zr alloy powder with a particle size distribution of 15–46 μm was applied in this study. Morphologies of the starting Al–Mg-Sc-Zr powder are shown in Fig. 1a and particle size distribution of the initial powder is provided in Fig. 1b. The chemical compositions of the initial powder are further listed in Table 1. Al–Mg-Sc-Zr specimens were processed using an SLM-150 machine. A 500 W fiber laser having a wavelength of 1.06 μm was utilized. The SLM process was conducted under an argon atmosphere with oxygen content less than 50 ppm to prevent oxidation. Substrate preheating function was not added in this experiment. Based on previous processing optimization [16], a laser power of 400 W, a scan speed of 600 mm/s, a hatch distance of 60 μm and a layer thickness of 30 μm were applied in this study. An island scanning strategy with a 37° rotation between two successive layers was utilized and a schematic of the island scanning strategy is depicted in Fig. 1c. In order to investigate the influence of island size d on SLM processed Al–Mg-Sc-Zr specimens, different island sizes of 1.2 mm, 2.4 mm, 3.6 mm, 4.8 mm, 6.0 mm and 7.2 mm were used in this study. Cubic specimens with a dimension of 10 mm × 10 mm × 10 mm and tensile specimens were fabricated by SLM. The Al–Mg-Sc-Zr tensile specimens processed by SLM with various island sizes are shown in Fig. 1d. After the SLM process, a post heat treatment of 325 °C/4h was applied for these specimens in a furnace under argon atmosphere.

2.2. Characterization of microstructures and mechanical properties

After the SLM process, the specimens were cut from the substrate and cleaned using distilled water and alcohol. Surface morphologies (also called surface finish) of the Al–Mg-Sc-Zr specimens were observed using a scanning electron microscopy (SEM, JSM-7600F, JOEL, Japan). Then the cubic specimens were ground using sandpapers from 60 to 3000 meshes and polished using silica suspension. The Archimedes method was used to obtain specific relative density values, and the image method is used to analyze the difference in the pore shape and size of the sample under different parameters using a PMG3 optical microscope (Olympus Corporation, Japan). Before microstructure observations, the specimens were etched by a solution consisting of HCl (0.15 mL), HF (0.1 mL), HNO_3 (0.25 mL) and distilled water (9.5 mL) for 30s. Microstructures of the Al–Mg-Sc-Zr specimens were characterized using an optical microscope and a scanning electron microscopy. The residual stress analyses were conducted using a Bruker D8 Advance X-ray diffraction (XRD) with a Cu Kα radiation at 30 mA and 40 kV. Diffraction angles (2θ) ranged from 20° to 90° with a scan speed of 4° per minute. Tensile tests were carried out at room temperature on a CMT5205 testing machine (MTS industrial systems, China) with a fixed strain rate of 2 mm/min. Tensile fractures were further observed by SEM. The scanning time under different island sizes was measured during the SLM process.

2.3. Electrochemical measurements

Before electrochemical tests, the tested surfaces (Building plane, XY-plane) of the Al–Mg-Sc-Zr specimens were grinded and polished. The exposed surface area of the specimens was approximately 1 cm^2. A 3.5 wt% NaCl solution was prepared for the electrochemical measurements using deionized water and analytical grade reagents to simulate the environment containing chloride ions. The electrochemical measurements were performed in 3.5 wt% NaCl solution on an electrochemical workstation (CHI660e, ChenHua, China) at room temperature. A conventional three-electrode cell system consisted of a working electrode

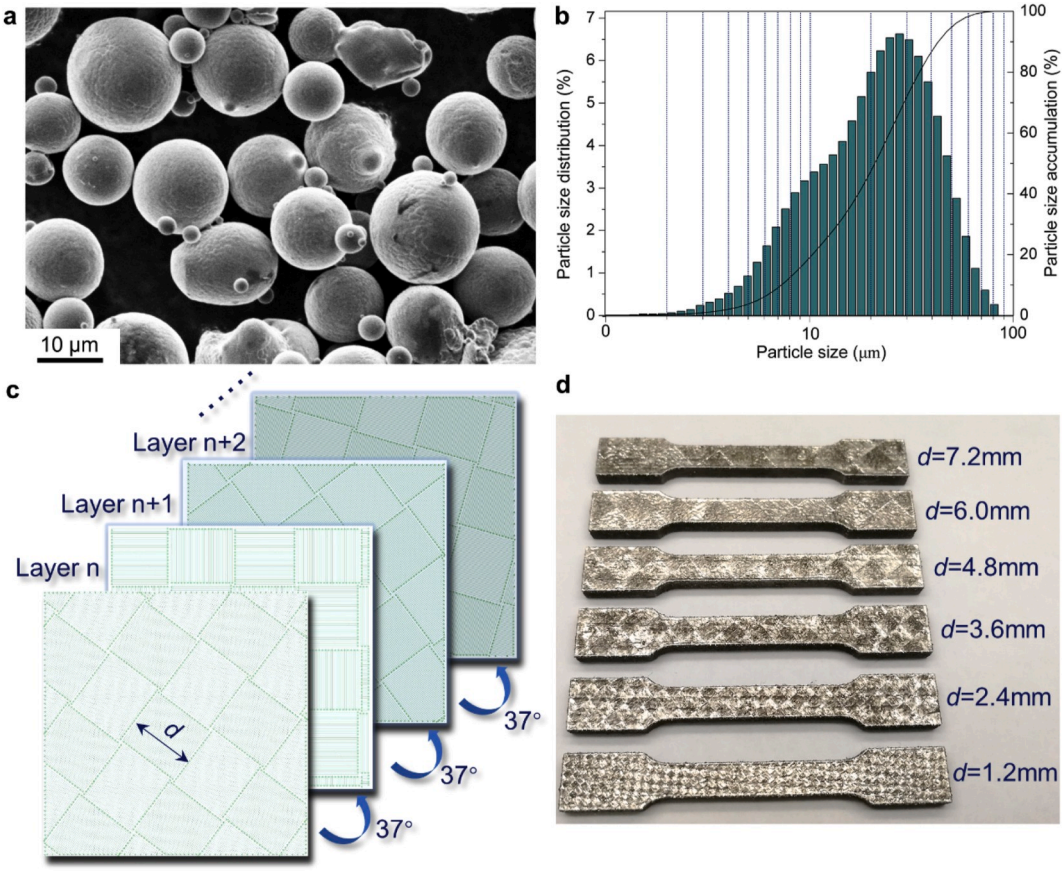

Fig. 1. (a) Morphology of the starting Al–Mg-Sc-Zr powder and (b) particle size distribution of the initial Al–Mg-Sc-Zr powder; (c) Schematic of the island scanning strategy with a 37° rotation angle between two neighboring layers, where *d* represents island size; (d) SLM produced Al–Mg-Sc-Zr tensile specimens with different island sizes.

Table 1
Chemical compositions of initial Al–Mg-Sc-Zr powder.

Element	Al	Mg	Sc	Zr	Cr	Cu	Fe	Mn	Ti
Contents (wt.%)	Balance	4.2	0.4	0.2	0.01	0.005	0.1	0.18	0.001

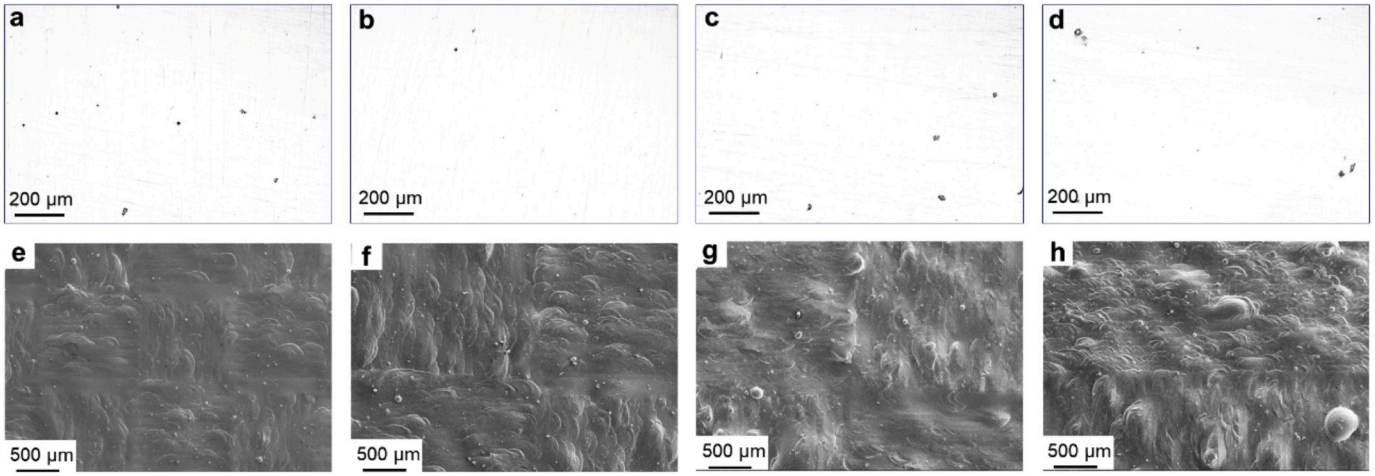

Fig. 2. Optical micrographs showing densification levels of SLM produced Al–Mg-Sc-Zr specimens using various island sizes: (a) 1.2 mm, (b) 2.4 mm, (c) 4.8 mm, (d) 7.2 mm; SEM micrographs revealing typical surface morphologies of SLM processed Al–Mg-Sc-Zr specimens with different island sizes: (e) 1.2 mm, (f) 2.4 mm, (g) 4.8 mm, (h) 7.2 mm.

(Al–Mg-Sc-Zr specimens), a counter electrode (platinum foil) and a reference electrode (saturated calomel electrode, SCE) was applied in this study. Before electrochemical impedance spectroscopy (EIS) tests and potentiodynamic polarization measurements, the tested surfaces of the Al–Mg-Sc-Zr specimens were immersed in the 3.5 wt% NaCl solution for sufficient time to reach a stable open circuit potential (OCP) value. The EIS measurements were conducted under a stabilized OCP value and the frequency was varied from 10^{-2} to 10^{5} Hz combined with an amplitude of 10 mV. The potentiodynamic polarization tests were measured from −0.4V to −1.7 V with a scanning speed of 2 mV/s. All electrochemical tests were repeated three times for data reproducibility.

3. Results

3.1. Densification behavior and surface morphology

Fig. 2a–d shows the cross-section optical images of the Al–Mg-Sc-Zr specimens processed by SLM with various island sizes. It can be found that the densification behavior, e.g. the residual porosity was slightly influenced by the applied island size. At a relatively small island size *d* of 1.2 mm, several micropores with an average size of 10 μm were generated and the relative density of the specimen was 99.1% (Fig. 2a). At a larger *d* of 2.4 mm, fewer micropores with a higher relative density of 99.6% were obtained (Fig. 2b). While as the island size further increased to 4.8 mm and 7.2 mm, the number of micropores increased and thereby the relative density of the SLM specimens reduced to 99.4% and 99.1%, respectively (Fig. 2c and d). For the Al–Mg-Sc-Zr specimens processed by SLM with various island sizes (1.2 mm–7.2 mm), no severe defects such as unmolten pores and cracks can be found. Despite the island size has an influence on residual porosity, the relative density for all the Al–Mg-Sc-Zr specimens was above 99%, indicating all specimens reached a high densification level under different island sizes. Fig. 2e and f provide the surface morphologies of the Al–Mg-Sc-Zr specimens processed by SLM with different island sizes. The surface of the Al–Mg-Sc-Zr specimen processed at an island size *d* of 1.2 mm was relatively smooth, showing no obvious pores or cracks were generated. Continuous scan tracks and island boundaries can also be identified on the surface (Fig. 2e). As the island size *d* increased, the surfaces gradually became irregular and several small-sized metallic balls were formed (Fig. 2f–h). At a relatively large island size *d* of 7.2 mm, the surface became quite irregular and large metallic balls with a mean size of 400 μm were observed, indicating the liquid solidification became significantly disorderly at a large island size *d* of 7.2 mm (Fig. 2h).

3.2. Microstructure development

Fig. 3 depicts the molten pool boundary features on the cross section of the Al–Mg-Sc-Zr specimens processed by SLM with different island sizes. It can be found that the molten pool configurations were considerably affected by the island size. At a moderate island sizes *d* of 2.4 mm and 4.8 mm (Fig. 3b and c), the molten pool configurations exhibited relatively regular layerwise characteristics with an average molten pool depth of ~50 μm, indicating the SLM processes were stable under $d =$ 2.4 mm and $d = 4.8$ mm. At a relatively small island size *d* of 1.2 mm, the molten pool became irregular and the depth of molten pool increased, indicating larger molten pools and more heat accumulation were generated at $d = 1.2$ mm compared to $d = 2.4$ mm and $d = 4.8$ mm. On increasing *d* to 7.2 mm, however, even more irregular molten pool features combined with deeper molten pool depth (~100 μm) were observed (Fig. 3d), suggesting a severe heat accumulation at the large island size $d = 7.2$ mm. Even key-hole can be found at $d = 7.2$ mm as shown in Fig. 3d [22]. Comparing the molten pool configurations of the Al–Mg-Sc-Zr specimens with different island sizes, it can be concluded that stable SLM processes were generated at $d = 2.4$ mm and $d = 4.8$ mm. At a small island size $d = 1.2$ mm or a large island size $d = 7.2$ mm, heat accumulation was generated especially for $d = 7.2$ mm, where the molten pool can penetrate several previous layers.

Fig. 4 shows backscattered SEM micrographs of the Al–Mg-Sc-Zr specimens processed by SLM with different island sizes. Typical fan-shell solidification microstructures were obtained for all specimens, which consisted of two different zones in a single molten pool: large columnar grains formed in the center of the molten pool and fine equiaxed grains generated along molten pool boundaries. The formation of equiaxed grains along the boundary of the molten pool was due to the presence of nucleating agents such as $Al_3(Sc,Zr)$ particles to refine the grains, while the formation of columnar grains in the middle of the molten pool was due to the thermal behavior during solidification [11,16]. It can be seen that bright contrast precipitations formed and agglomerated in the fine equiaxed regions and along columnar grain boundaries (Fig. 4). In general, the laser additive manufacturing processed Al–Mg-Sc-Zr alloy

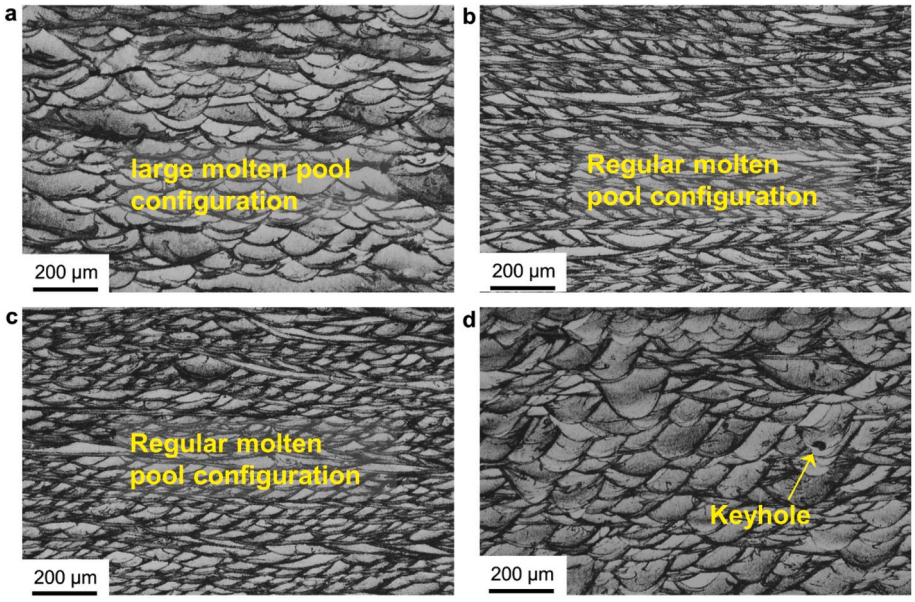

Fig. 3. Optical micrographs of etched vertical section of SLM produced Al–Mg-Sc-Zr specimens with different island sizes: (a) $d = 1.2$ mm, (b) $d = 2.4$ mm, (c) $d =$ 4.8 mm, (d) $d = 7.2$ mm, showing molten pool configurations were different under various island sizes.

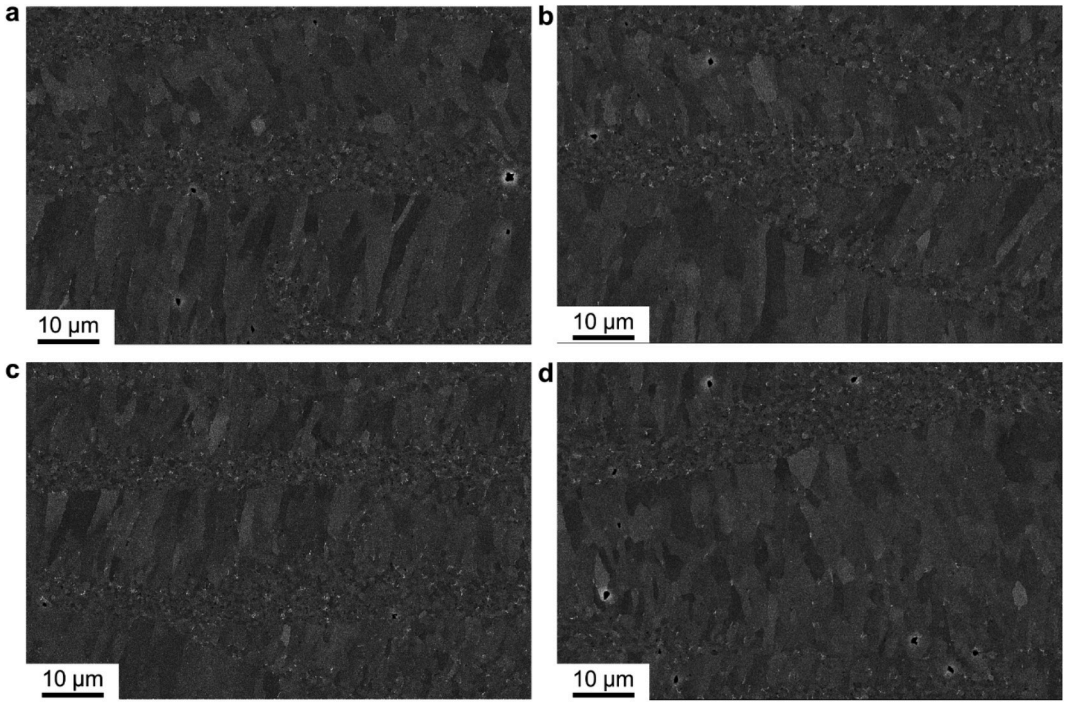

Fig. 4. Backscatter SEM micrographs showing the cross section of SLM processed Al–Mg-Sc-Zr specimens with various island sizes after heat treated at 325 °C for 4 h: (a) $d = 1.2$ mm, (b) $d = 2.4$ mm, (c) $d = 4.8$ mm, (d) $d = 7.2$ mm. Typical fanshell solidification structure consisting of elongated grains and equiaxed grains were visible for all specimens. $Al_3(Sc,Zr)$ precipitations (white points) preferred locating in the fine grained area along the molten pool boundaries.

mainly includes two precipitates, $Al_3(Sc,Zr)$ and Al–Mg oxide. In backscattered SEM detection, the element with higher atomic number tends to show a brighter contrast, thus these bright contract precipitations should be $Al_3(Sc,Zr)$ particles, which were formed during the SLM process and the aging process. Comparing the grain size distribution among different specimens, it can be found that the fine-grain area of the specimens with $d = 2.4$ mm and $d = 4.8$ mm was larger than that of $d = 1.2$ mm and $d = 7.2$ mm, which may be related to the different molten pool configurations as shown in Fig. 3.

3.3. Residual stress analysis

Typical XRD spectra of the Al–Mg-Sc-Zr specimens processed by SLM with different island sizes are shown in Fig. 5a. Diffraction peaks corresponding to face-centered cubic (fcc) α-Al (JCPDS Card No. 04–0787) can be identified for all specimens. Based on the XRD results, one method suitable to characterize and quantify the microstrains and residual stress of the Al–Mg-Sc-Zr specimens was the Williamson-Hall method [23–25]. If the peak broadening was only induced by variations of interplanar crystal spacing (caused by lattice distortions, dislocations or solid solution), the effective average microstrain, e (a parameter that represents the standard deviation of the microstrain distribution) could be calculated by the integral breadth of the *hkl* reflection [26,27]:

$$\delta_{e,hkl} = 4e \tan \theta_{\max,hkl} \quad (1)$$

where $\theta_{\max,hkl}$ is the position of α-Al diffraction peaks. If the peak broadening was solely induced by a reduction of the size of coherently diffracting domains, the integral breadth of the reflection with Laue indices, *hkl* can be given by Ref. [26,27]:

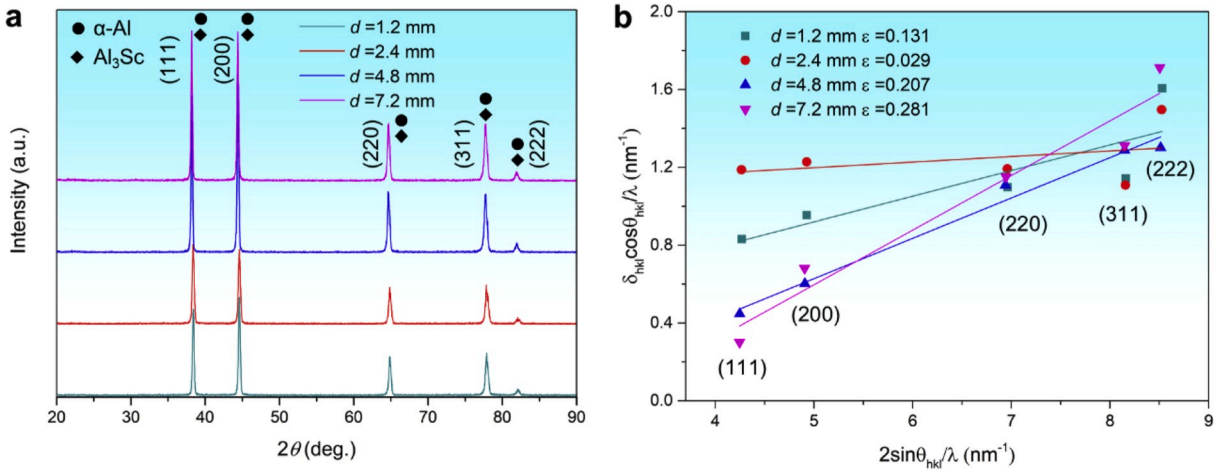

Fig. 5. (a) XRD results of SLM produced Al–Mg-Sc-Zr specimens with various island sizes. (b) Williamson-Hall plots for SLM produced Al–Mg-Sc-Zr specimens with different island sizes based on XRD results. The solid lines are the linear fits based on a least squares method and the slope ε represents the residual stress level.

$$\delta_{D,hkl} = \frac{\lambda}{D \cos \theta_{\max,hkl}} \quad (2)$$

where D is the average size of the coherently diffracting domains. λ is the wavelength applied in XRD measurements. Based on Williamson-Hall's theory, both contributions to the overall peak broadening increased linearly. Thus total physical broadening consistd of size and strain can be provided as [26,27]:

$$\frac{\delta_{hkl} \cos \theta_{\max,hkl}}{\lambda} = \frac{1}{D} + \frac{4e \sin \theta_{\max,hkl}}{\lambda} \quad (3)$$

where δ_{hkl} is the integral breadth. In this study, D represents the grain size of the Al–Mg-Sc-Zr specimens processed by SLM using different island sizes. Previous research indicated that the influence of D on peak broadening was negligible if the grain size exceeds 100 nm [28]. For the SLM produced Al–Mg-Sc-Zr specimens, the grain size was generally above 2 μm as shown in Fig. 4, indicating $1/D$ can be ignored. Plotting (δ_{hkl} cos$\theta_{\max,hkl}/\lambda$) vs. (4sin$\theta_{\max,hkl}/\lambda$) can yield a straight line with a slope ε, which represented the value of average microstrain e. While the average microstrain can reflect the residual stress level to a certain extent of the SLM processed part. The calculated results based on the XRD measurements is shown in Fig. 5b and the solid lines are the linear fits according to the least squares method. It can be seen clearly that the Al–Mg-Sc-Zr specimen produced using an island size d of 2.4 mm exhibited a minimum slope ($\varepsilon = 0.029$), suggesting minimum residual stress was obtained at this situation. As the island size d increased to 4.8 mm and 7.2 mm, the slopes were increased to 0.207 and 0.281, respectively. Thus the residual stress of the SLM processed Al–Mg-Sc-Zr specimens was increased as the island size d increased. However, at a relatively small island size d of 1.2 mm, the slope was also increased ($\varepsilon = 0.131$) compared to $d = 2.4$ mm, indicating the residual stress was also increased at a relatively small island size.

3.4. Mechanical properties

Room temperature tensile tests were conducted on the Al–Mg-Sc-Zr specimens processed by SLM using different island sizes and the results are shown in Fig. 6.

Fig. 6a shows the stress-strain curves for the SLM produced Al–Mg-Sc-Zr specimens with various island sizes and the elastic stage of the curves is further provided inset Fig. 6a. Mechanical performance tests for specimens with different island sizes were repeated at least three times for data reproducibility. In order not to make the curves too confusing, we provide one of them for comparison. It seems that the influence of island size on the mechanical properties was limited. The ultimate tensile strength for all specimens with different island sizes exceeded 480 MPa and elongations mainly ranged between 10%~11%. Detail results of the ultimate tensile strength (σ_{UTS}), yield strength ($\sigma_{0.2}$) and elastic modulus (E) of the Al–Mg-Sc-Zr specimens processed by SLM using different island sizes are further depicted in Fig. 6b. For ultimate tensile strength, there was no obvious tendency can be concluded and the maximum σ_{UTS} (502.6 MPa) was obtained at $d = 7.2$ mm. Yield strength of 463.2 Mpa was generated at $d = 4.8$ mm and the $\sigma_{0.2}$ of other specimens was around 440 MPa. The elastic modulus E of all Al–Mg-Sc-Zr specimens processed by SLM using different island sizes were varied between 60–65 GPa. Based on the above analyzes, the influence of the island size on tensile properties was not significant and it seems like superior mechanical properties were obtained at $d = 4.8$ mm, where a higher elongation of 11.7% and a higher yield strength of 463.2 MPa were generated.

In order to further analyze the fracture mechanism, fracture morphologies of the Al–Mg-Sc-Zr specimens processed by SLM using different island sizes are presented in Fig. 7. Relatively rough fracture surfaces were obtained for all specimens, where non-uniform dimples with no cleavage planes can be identified. There were no apparent differences in fracture morphologies that can be identified for the Al–Mg-Sc-Zr specimens processed using various island sizes, which were consistent with the results of the tensile tests.

3.5. Corrosion properties

Fig. 8 shows a series of potentiodynamic polarization curves of the Al–Mg-Sc-Zr specimens processed by SLM using different island sizes in 3.5 wt% NaCl solution at room temperature. Corrosion potentials (E_{corr}) around −1500 mV combined with passive regions extended from −1400 mV to −700 mV were obtained for the specimens, indicating typical passive behaviors were generated. In addition, it can be seen that the corrosion current density rapidly increased in the anodic branch of the polarization curves for all Al–Mg-Sc-Zr specimens, indicating pitting corrosion was generated. Pitting corrosion generally related to the breakdown of the passive films formed on the surface, which was attacked by chloride [29]. As an essential electrochemical parameter, pitting potential (E_{pit}) can be used to evaluate the pitting initiation susceptibility for aluminum alloy. As marked in Fig. 8 and provided in Table 2, the E_{pit} values of the Al–Mg-Sc-Zr specimens processed by SLM using different island sizes were ranked in following orders: 4.8 mm > 2.4 mm > 1.2 mm > 7.2 mm, where a maximum E_{pit} (−573 ± 12 mV) was obtained at $d = 4.8$ mm. In general, a higher E_{pit} indicates a better pitting resistance. Thus the specimen with an island size d of 4.8 mm exhibited the highest pitting resistance compared to other specimens. As the island size decreased, the pitting resistance was gradually decreased and the pitting corrosion was more severe at a relatively large island

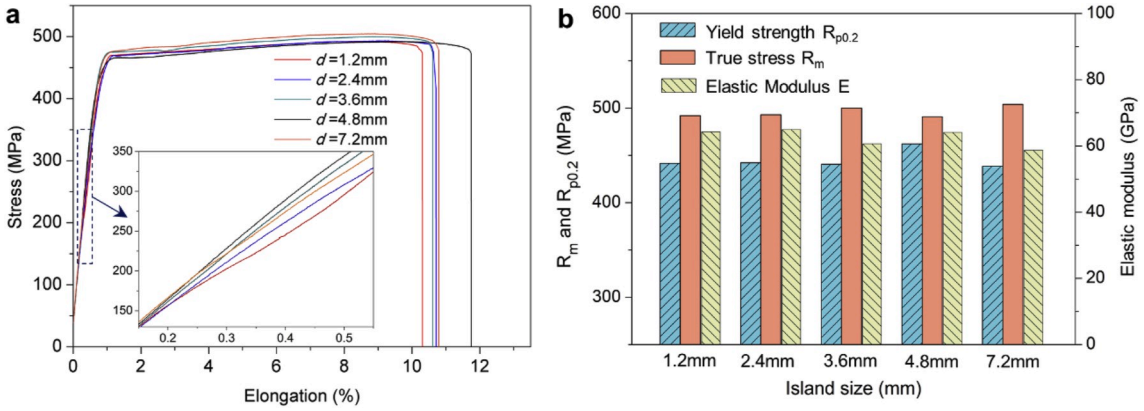

Fig. 6. (a) Stress strain curves for SLM produced Al–Mg-Sc-Zr specimens with various island sizes after heat treated at 325 °C for 4 h. The inset shows the elastic stage curves during tensile tests. (b) True ultimate tensile strength R_m, yield strength $R_{p0.2}$ and elastic modulus E for SLM produced Al–Mg-Sc-Zr specimens with different island sizes.

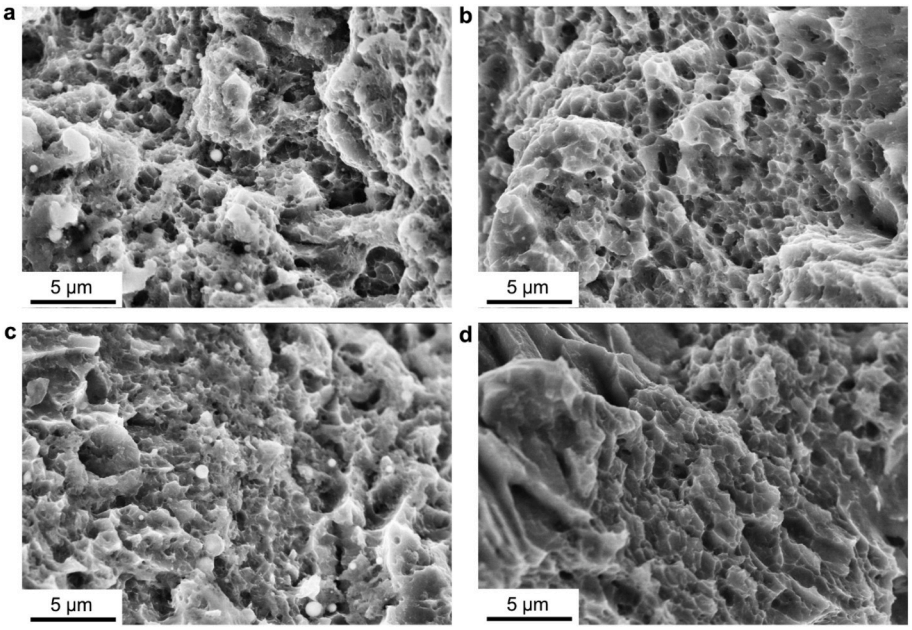

Fig. 7. Fracture surfaces of SLM produced Al–Mg-Sc-Zr specimens with various island sizes after heat treated at 325 °C for 4 h: (a) d = 1.2 mm, (b) d = 2.4 mm, (c) d = 4.8 mm, (d) d = 7.2 mm.

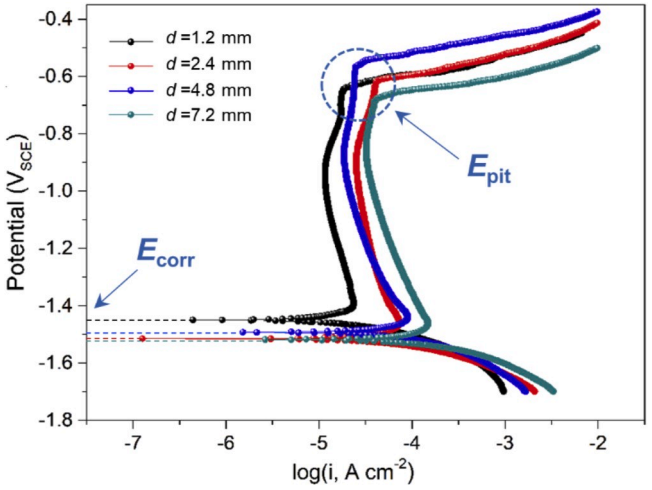

Fig. 8. Potentiodynamic curves for SLM produced Al–Mg-Sc-Zr specimens with different island sizes in 3.5 wt% NaCl solution at room temperature.

Table 2
Electrochemical measurements of the polarization curves for SLM produced Al–Mg-Sc-Zr specimens with various island sizes.

Island sizes (d)	E_{pit} (mV vs SCE)	I_{corr} (A cm^{-2})
1.2 mm	−644 ± 10	(5.12 ± 0.17) × 10^{-5}
2.4 mm	−616 ± 15	(9.37 ± 0.22) × 10^{-5}
4.8 mm	−573 ± 12	(6.82 ± 0.13) × 10^{-6}
7.2 mm	−674 ± 8	(3.20 ± 0.15) × 10^{-4}

size. Corrosion current density (i_{corr}), which can be calculated from polarization curves using the Tafel slope extrapolation method, is another important parameter to evaluate the corrosion rate and corrosion resistance. As provided in Tabel 2, the minimum i_{corr} of (6.28 ± 0.13) × 10^{-6} A cm^{-2} was obtained for the specimen processed with an island size d of 4.8 mm, which was consistent with the E_{pit} results. Thus it can be concluded that the Al–Mg-Sc-Zr specimen processed by SLM using a moderate island size d of 4.8 mm possessed a superior corrosion resistance. An elevated or decreased island size led to a reduction of pitting resistance and corrosion resistance.

EIS measurements were applied to investigate the surface condition of the Al–Mg-Sc-Zr specimens processed by SLM using different island sizes and the results are provided in Fig. 9. As shown in the Nyquist plot (Fig. 9a), two typical capacitive loops were observed for all specimens. In order to further identify the loop radius of different specimens, the inset of Fig. 9a shows the partial magnification of the Nyquist plot. It can be seen that the Al–Mg-Sc-Zr specimen processed with an island size d of 4.8 mm exhibited the largest radius compared to other specimens and, the specimen with an island size d of 7.2 mm exhibited the smallest radius, indicating a superior corrosion resistance was obtained for the specimen with an island size of 4.8 mm. In the phase angle Bode plot (Fig. 9b), two peaks consisted of one peak (phase angles close ~75°) at the middle frequency and another peak (phase angles around 20–35°) at the low frequency were obtained for all specimens, which were consistent with the two time constants obtained in the Nyquist plot. Therefore, an equivalent circuit model with two time constants was applied to fit the EIS results (Fig. 9d). In the equivalent circuit, R_s represented the solution resistance, R_f and CPE_1 represented the film resistance and film capacitance, respectively. R_{ct} and CPE_2 referred to the charge transfer resistance and foible layer capacitance, respectively. Here, a constant phase element (CPE_1) was conducted to analyze the capacitive behavior on the passive film and the impedance of CPE can be described by Ref. [30]:

$$Z_{CPE} = \frac{1}{Q(j\omega)^n}(-1 \le n \le 1) \quad (4)$$

where ω represents the angular frequency, Q represents the CPE constant, $j^2 = -1$ represents the imaginary number and n represents the CPE exponent. Furthermore, the overall impedance of the electrode system can be defined by Ref. [31]:

$$Z = R_s + \frac{1}{1/R_p + Q(j\omega)^{-n}} \quad (5)$$

The fitting results of the EIS tests are summarized in Table 3. The value of R_f ranked in the following order: 1.2 mm < 7.2 mm < 2.4 mm < 4.8 mm. The Al–Mg-Sc-Zr specimen processed using an island size d of

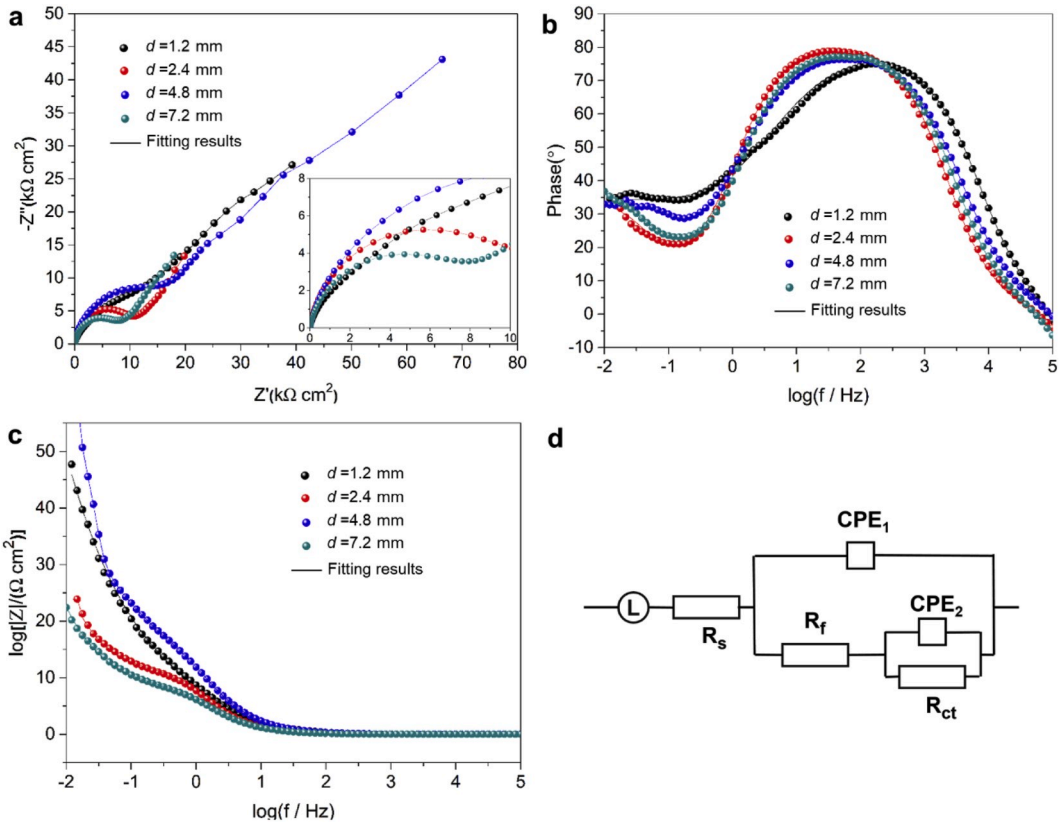

Fig. 9. EIS measurements of SLM produced Al–Mg-Sc-Zr specimens with different island sizes tested in 3.5wt% NaCl solution at room temperature: (a) Nyquist plot; (b) phase angle Bode plot and (c) impedance Bode plot; (d) equivalent circuit model.

Table 3
Equivalent circuit parameters for SLM produced Al–Mg-Sc-Zr specimens with different island sizes in 3.5 wt% NaCl solution.

Island sizes	$\chi^2 \times 10^{-4}$ Chi-squared values	R_f (kΩ cm^2)	$CPE_1 \times 10^{-6}$ (F cm^{-2})	n_1	$CPE_2 \times 10^{-4}$ (F cm^{-2})	n_2
1.2 mm	5.86 ± 0.13	5.15 ± 0.16	10.16 ± 0.28	0.87 ± 0.03	64.94 ± 1.67	0.40 ± 0.04
2.4 mm	5.28 ± 0.21	11.91 ± 0.21	16.67 ± 0.37	0.91 ± 0.04	4.07 ± 0.78	0.78 ± 0.02
4.8 mm	4.26 ± 0.15	20.11 ± 0.32	10.02 ± 0.26	0.88 ± 0.02	1.35 ± 0.56	0.87 ± 0.01
7.2 mm	2.51 ± 0.17	8.86 ± 0.19	19.58 ± 0.44	0.89 ± 0.03	3.61 ± 0.39	0.69 ± 0.03

4.8 mm exhibited the highest R_f value of 20.11 ± 0.32 kΩ cm^2 compared to other specimens, suggesting the specimen with an island size of 4.8 mm possessed a superior corrosion resistance. As the island size *d* decreased to 1.2 mm and 2.4 mm or increased to 7.2 mm, the corrosion resistance decreased, which was a good agreement with the measurements in polarization tests. In addition, SEM micrographs of the corrosion morphologies on the XY-plane (electrochemical tested plane) of the Al–Mg-Sc-Zr specimens with different island sizes after potentiodynamic tests are shown in Fig. 10. Typical morphologies corresponding to pitting corrosions were observed for all specimens. Massive and deep pits were generated for specimens with an island size of 1.2 mm and 7.2 mm (Fig. 10a and d), indicating an inferior corrosion resistance for these specimens. At an island size *d* of 2.4 mm, the amount and the size of the pits were decreased, indicating the corrosion resistance was enhanced to some extent (Fig. 10b). The smallest corrosion area was obtained at an island size *d* of 4.8 mm and the size of the pits was much smaller at this situation (Fig. 10c).

4. Discussion

4.1. The influence of island size on scanning time

The average time required to scan a 10 mm × 10 mm area under the same laser scan speed of 600 mm/s with different island sizes is provided in Fig. 11, which shows the effect of the island size on scanning time. The shortest scanning time of 3.1 s was recorded for the largest island size *d* of 7.2 mm. As the island size decreased, the scanning time was gradually increased and the longest scanning time of 4.6 s was obtained for the smallest island size *d* of 1.2 mm, which was 48% longer than that of the island size *d* of 7.2 mm. The different scanning times under different island sizes can be explained by the increment of the laser beam "jump" time as the island size decreased. Meanwhile, more overlap regions at island borders were generated at a smaller island size, leading to the increment of total laser scanning length. Thus the island size significantly affected the laser scanning time and higher processing efficiency was obtained at a larger island size.

4.2. The influence of island size on densification behavior

As we discussed above, the surface morphologies of the Al–Mg-Sc-Zr specimens deteriorated as island size increased (Fig. 2e–h). Generally, due to the track-by-track manufacturing characteristic of the SLM process, the previous track has a preheating effect on the next track, making the surrounding powder heat up before laser scanning. Thus the temperature gradient was decreased as the preheating effect increased [20, 21]. When the island size is small, the laser scanning vector inside an island is relatively short and the interval time between adjacent scanning tracks is significantly reduced. Thus an enhanced preheating effect is generated, leading to a decreased temperature gradient and attendant elevated melt stability. This is the reason for the enhanced surface

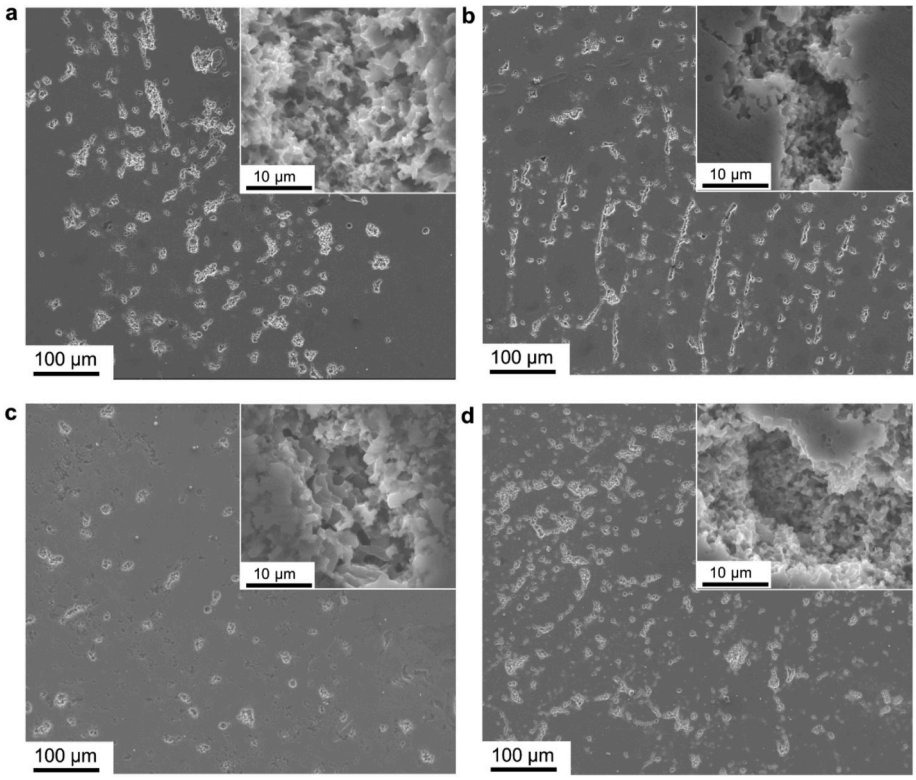

Fig. 10. SEM micrographs of corrosion morphologies on the surfaces of SLM produced Al–Mg-Sc-Zr specimens with different island sizes after potentiodynamic tests: (a) $d = 1.2$ mm, (b) $d = 2.4$ mm, (c) $d = 4.8$ mm, (d) $d = 7.2$ mm.

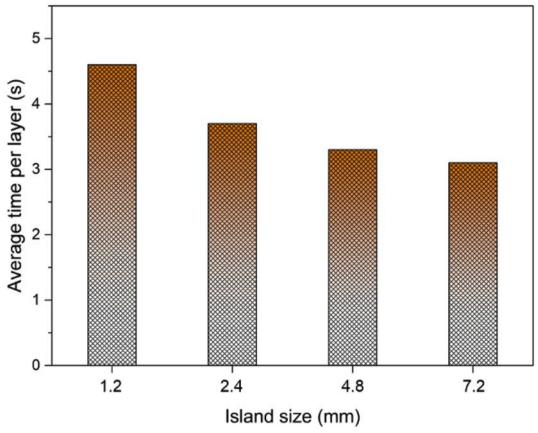

Fig. 11. Average times required to scan a 10 mm × 10 mm area under the same laser scan speed of 600 mm/s with different island sizes, showing a smaller island size leads to longer processing time.

qualities as the island size reduced. Based on the process optimizations of previous work [16], all specimens with different island sizes reached a relative high densification level. Only a few micropores can be observed as shown in Fig. 2a-d, and the island size has a slight effect on the porosity. The slightly higher porosity under a small island size of 1.2 mm can be attributed to the increment of overlap regions between adjacent islands. In order to avoid the formation of un-melted powder at the island borders, an overlap region with a width of 60 μm was applied between islands. These overlap regions were scanned twice by the laser beam, leading to excessive energy input. Low melting point elements including Al and Mg are easy to evaporate at the overlap region and form micropores inside the specimen. Thus the porosity was increased at a relatively small island size. At a relatively large island size, due to the reduced preheating effect, a large temperature gradient is generated within the molten pool, leading to a more significant Marangoni convection and an increased melt instability. Thus defects including micropores are easy to form at a relatively large island size. It is interesting to found that the molten pool size is considerably influenced by the island size, where the depth of the molten pool increased at a relatively small island size of 1.2 mm and a relatively large island size of 7.2 mm (Fig. 3). Based on previous works [20], it is believed that heat accumulation and thermal distribution can be influenced by the island size. Parry [32] and Haider Ali [33] have proved that a high average temperature within the molten pool is generated when a small island size is applied, which leads to the increment of melt depth. Besides, as we discussed above, the scanning time and total laser scanning length increased as the island size reduced, resulting in server heat accumulation inside the specimen, which is also one of the reasons for the large molten depth. As for a relatively large island size, due to the increase of the scanning time of a single area, the thermal influence time of duration of the previous and subsequent melt tracks increases, resulting in an increase in the heat accumulation effect. Besides, the temperature gradient plays a key role in the formation of the molten pool. The temperature gradient within the molten pool affects the surface tension gradient and Marangoni convection [34]. Thus a drastic Marangoni flow was generated at a large island size due to the enhanced temperature gradient, leading to a key-hole model molten pool with a large molten depth (Fig. 3d) [22].

4.3. The influence of island size on microstructure and tensile properties

Generally, for Sc and Zr modified Al–Mg alloy processed by SLM, grain size distribution and $Al_3(Sc,Zr)$ precipitation are the most important microstructural factors [35,36]. It seems that the microstructures of the Al–Mg-Sc-Zr specimens processed by SLM using various island sizes show no significant differences in grain size distributions and precipitations inside a single molten pool (Fig. 4). Equiaxed and fine grains

along molten pool boundaries combined with coarser and elongated grains in the center of the molten pool were generated for all Al–Mg-Sc-Zr specimens. The formation mechanism of the microstructure has discussed in previous works, which relates to oxide particles and temperature gradients. It is well known that tensile properties are influenced by many factors, including densification behaviors, grain size distribution, defects, precipitations, etc. [11,16]. Since the microstructures including grain size distribution and precipitation for all Al–Mg-Sc-Zr specimens are very similar and all specimens reach a high densification level above 99%, the influence of island size on the tensile properties is limited. High ultimate tensile strengths of 500 MPa combined with elongation above 10% were obtained for all specimens. This conclusion is consistent with previous work [20], which indicates there is no significant influence of island size on the mechanical properties of SLM processed IN718 alloy.

4.4. The influence of island size on residual stress

Generally, complex stresses are generated in the SLM process due to a tendency of the cool-down phase of the subsequent layer to shrink, while such a deformation is restricted by the previous adjacent layer. Thus tensile stress in the subsequent layer and compressive stress in the previous layer are formed. These residual stresses can significantly affect the performance and service life of the components processed by the SLM process. Island laser scanning strategy has approved to be one of the significant methods to reduce residual stress and, the residual stress was decreased as island size reduced [33,37,38]. This work presents a similar result when the island size is above 2.4 mm, where the residual stress is increased as the island size increased (Fig. 5). Generally, a long scanning track combined with a weakened pre-heating effect is generated when a large island size is applied, inducing a high temperature gradient and correspondingly high residual stress. Besides, the overlap regions at island borders usually act as stress release areas due to the laser re-scanning and preheating effect from the previous island [21]. As the island size reduced, the overlap regions (i.e. the stress release areas) at the borders of the island increased, leading to the decrease of the residual stress of the SLM processed Al–Mg-Sc-Zr specimens. However, as the island size decreased to 1.2 mm, a high level of residual stress was generated inside the specimen, indicating the residual stress is increased at a relatively small island size. Similar results were also suggested by Lu [20], who found cracks were formed at an island size of 2 mm. At a relatively small island size, the total laser scanning length is increased due to the massive overlap regions, leading to the scanning time of a single layer is significantly increased compared to that at a large island size (i.e. 4.6s for an island size d of 1.2 mm and 3.1 for an island size d of 7.2 mm, Fig. 11). Excessive laser energy is inputted at a relatively small island size, resulting in a high level of residual heat effect, which can also be proved from the increased molten pool depth (Fig. 3). Thus increased residual stress is generated at a relatively small island size and, the residual stresses under different island sizes rank as follows: 2.4 mm $<$ 1.2 mm $<$ 4.8 mm $<$ 7.2 mm. As analyzed above, the island size considerably affects the residual stress of the Al–Mg-Sc-Zr specimens processed by SLM. From a perspective of the residual stress, the optimal island size is 2.4 mm.

4.5. The influence of island size on corrosion behaviors

Based on the electrochemical measurements, the Al–Mg-Sc-Zr specimen processed by SLM using an island size of 4.8 mm exhibits a superior corrosion resistance combined with the minimum i_{corr} of $(6.82 \pm 0.13) \times 10^{-6}$ A cm^{-2}. An increased or decreased island size leads to inferior corrosion resistance. For SLM fabricated aluminum alloy, the molten pool boundaries are generally acted as weakened areas with inferior corrosion resistance. There are two reasons for the decrease in corrosion resistance at the molten pool boundary. One is the refinement of grains at the boundary of the molten pool lead to the high grain boundary density. Thus the reaction activity along the molten pool is strong and corrosion is easy to occur. The other is that the $Al_3(Sc,Zr)$ precipitates at the boundary of the molten pool are dense, and these precipitates can easily act as microelectrodes to accelerate the corrosion process [39–41]. Since there are no significant differences in the grain size distribution and primary precipitation for the Al–Mg-Sc-Zr specimens processed using different island sizes, the molten boundary configuration (molten boundary density) plays a key role to affect the corrosion resistance of the Al–Mg-Sc-Zr specimens. Therefore, in order to further reveal the corrosion mechanism of the Al–Mg-Sc-Zr specimens processed by SLM using different island sizes, SEM images of the molten pool configurations on the XY-planes (corrosion tested plane) of the specimens are provided in Fig. 12. It is obvious that the island size significantly influences the molten pool configurations. Schematic representations of the molten pool configurations on the XY-planes of the Al–Mg-Sc-Zr specimens processed using different island sizes are illustrated in Fig. 13. At a relatively small island size of 1.2 mm, a regular molten pool configuration combined with massive island borders can be identified (Figs. 12a and 13a), leading to a high molten pool boundary density. As the island size increased to 2.4 mm, the number of island borders reduced, resulting in the molten pool boundary density decreased (Figs. 12b and 13b). At a further large island size of 4.8 mm, the influence of the island border is negligible while a few ellipsoidal molten pools were observed (Figs. 12c and 13c). These ellipsoidal molten pools were the bottom of the above layer, leading to the molten pool density increased. An extremely disordered molten pool configuration with numerous ellipsoidal molten pools was generated when a relatively large island size of 7.2 mm was applied (Figs. 12d and 13d), which was caused by the high temperature gradient and resultant high molten depth. As such, a high molten pool boundary density was obtained at an island size of 7.2 mm. Thus the molten pool boundary density was increased at a small island size due to the massive island borders and, also increased at a large island size owing to the enhanced disorder with numerous ellipsoidal molten pools. Therefore, inferior corrosion resistances were obtained at a relatively small or large island size and, superior corrosion resistance was generated for the Al–Mg-Sc-Zr specimen with an island size of 4.8 mm.

In conclusion, the island size has significant effects on the surface morphologies, molten pool configurations, residual stresses and corrosion resistances of SLM processed Al–Mg-Sc-Zr alloy. While the influence of island size on densification behavior, grain size distribution, and tensile properties is limited. Based on the above analyzes, a moderate island size between 3 and 5 mm is suggested for SLM processed Al–Mg-Sc-Zr alloy.

5. Conclusion

In this research, the influence of island size on SLM processed Al–Mg-Sc-Zr alloy was systemically studied. The surface morphologies, microstructures, tensile properties, residual stresses and corrosion resistances of the Al–Mg-Sc-Zr specimens processed by SLM using different island sizes were characterized and analyzed. The main conclusions are summarized as follows:

(1) All specimens reached a high densification level above 99% under different island sizes and, there was a slight influence of island size on porosity. As the island size decreased from 7.2 mm to 1.2 mm, the surface quality was gradually enhanced due to the reduced scanning length. A relatively smooth surface was obtained at an island size of 1.2 mm due to the enhanced preheating effect from previous tracks. The influence of island size on the grain size distribution and precipitation was not significant.
(2) The residual stresses of the Al–Mg-Sc-Zr specimens processed by SLM using different island sizes ranked in the following order: 2.4 mm $<$ 1.2 mm $<$ 4.8 mm $<$ 7.2 mm. The minimum residual

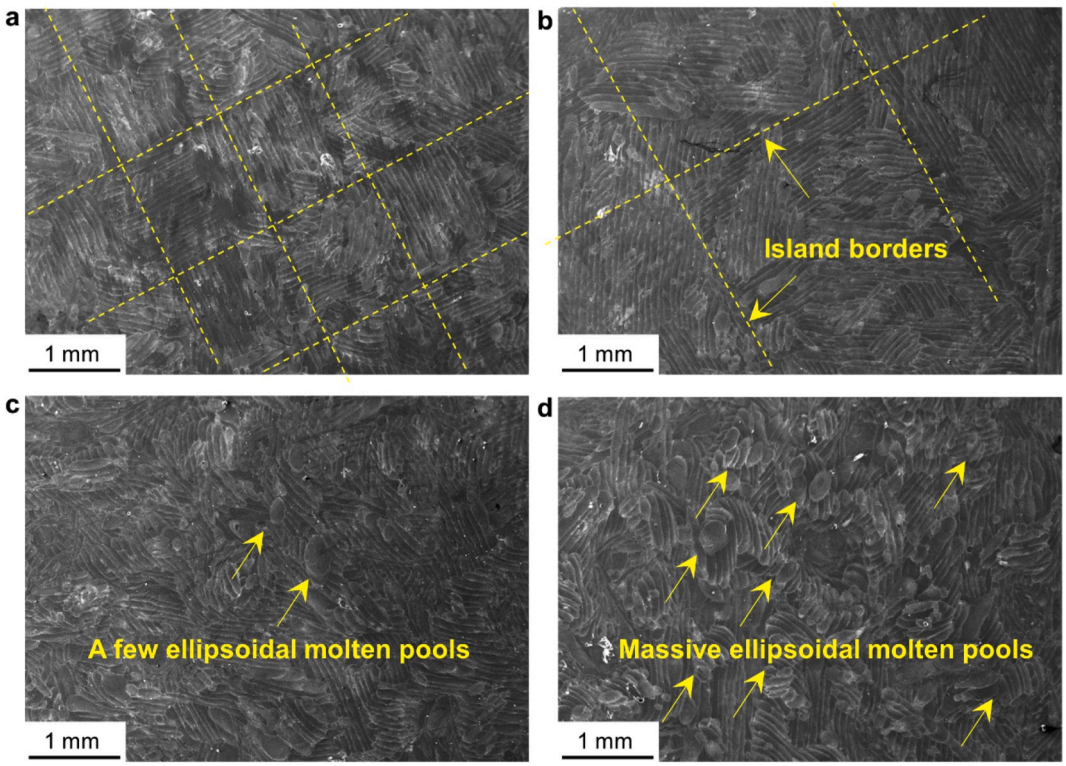

Fig. 12. SEM images on the corrosion tested planes (building planes) of SLM produced Al–Mg-Sc-Zr specimens with different island sizes: (a) $d = 1.2$ mm, (b) $d = 2.4$ mm, (c) $d = 4.8$ mm, (d) $d = 7.2$ mm, showing molten pool configurations on building planes are different under various island sizes.

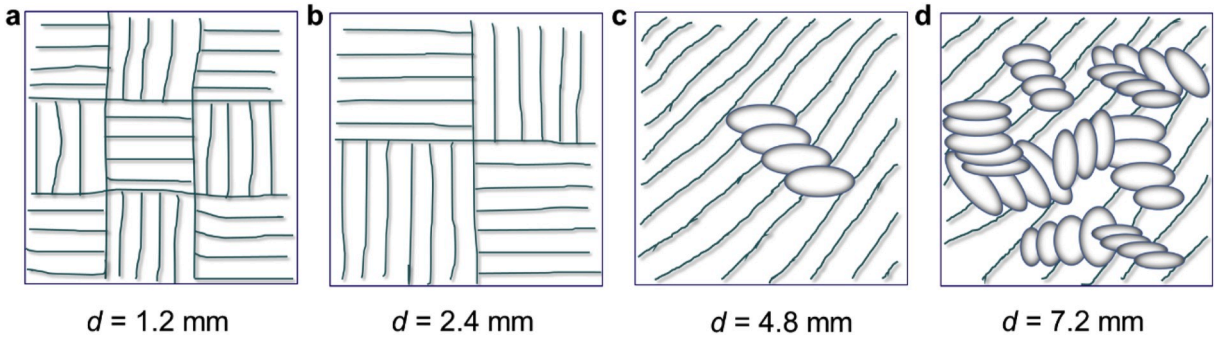

Fig. 13. Schematic representation of molten pool configurations on building planes of SLM produced Al–Mg-Sc-Zr specimens with various island sizes: (a) $d = 1.2$ mm, (b) $d = 2.4$ mm, (c) $d = 4.8$ mm, (d) $d = 7.2$ mm.

stress ($\varepsilon = 0.029$) was obtained at a moderate island size of 2.4 mm. High residual stress was generated at a large island size due to the increased length of individual tracks and resultantly increased temperature gradient. At a relatively small island size of 1.2 mm, the residual stress was also increased, which related to the increment of the total scanning length and scanning time.

(3) Superior corrosion resistance with a minimum i_{corr} of $(6.82 \pm 0.13) \times 10^{-6}$ A cm^{-2} was generated at a moderated island size of 4.8 mm. The corrosion behaviors of the Al–Mg-Sc-Zr specimens under different island sizes highly related to the molten pool configurations. At a small island size, the massive island borders led to the increased molten pool boundary density. The molten pool boundary density was also increased at a relatively large island size due to the enhanced disorder with numerous ellipsoidal molten pools

Data availability

The raw/processed data required to reproduce these findings cannot be shared at this time as the data also forms part of an ongoing study.

Declaration of competing interest

This paper mainly focused on the influence of island size on the microstructure features, residual stresses and properties of Al–Mg-Sc-Zr alloy processed by selective laser melting. We declare that we do not have any commercial or associative interest that represents a conflict of interest in connection with the work submitted.

CRediT authorship contribution statement

Han Zhang: Investigation, Writing - original draft. **Dongdong Gu:** Funding acquisition, Writing - review & editing. **Donghua Dai:** Data curation, Methodology. **Chenglong Ma:** Data curation, Methodology.

Yuxin Li: Investigation. **Ruolin Peng:** Data curation. **Shuhui Li:** Data curation. **Gang Liu:** Conceptualization. **Biqi Yang:** Conceptualization.

Acknowledgements

We are grateful for the financial support from National Natural Science Foundation of China (No. 51735005); National Key Research and Development Program "Additive Manufacturing and Laser Manufacturing" (Nos. 2016YFB1100101, 2018YFB1106302); National Natural Science Foundation of China for Creative Research Groups (Grant No. 51921003); The 15th Batch of "Six Talents Peaks" Innovative Talents Team Program "Laser Precise Additive Manufacturing of Structure-Performance Integrated Lightweight Alloy Components" (No. TD-GDZB-001); 2017 Excellent Scientific and Technological Innovation Teams of Universities in Jiangsu "Laser Additive Manufacturing Technologies for Metallic Components" funded by Jiangsu Provincial Department of Education of China.

References

[1] L. Thijs, K. Kempen, J.P. Kruth, J. Van Humbeeck, Fine-structured aluminum products with controllable texture by selective laser melting of pre-alloyed AlSi10Mg powder, Acta Mater. 61 (2013) 1809–1819, https://doi.org/10.1016/j.actamat.2012.11.052.

[2] D. Gu, X. Rao, D. Dai, C. Ma, L. Xi, K. Lin, Laser additive manufacturing of carbon nanotubes (CNTs) reinforced aluminum matrix nanocomposites: processing optimization, microstructure evolution and mechanical properties, Addit. Manuf. 29 (2019) 100801, https://doi.org/10.1016/j.addma.2019.100801.

[3] D. Wang, Y. Wang, Y. Yang, J. Lu, Z. Xu, S. Li, K. Lin, D. Zhang, Research on design optimization and manufacturing of coating pipes for automobile seal based on selective laser melting, J. Mater. Process. Technol. 273 (2019) 116227.

[4] M.J. Bermingham, D.H. Stjohn, J. Krynen, S. Tedman-jones, M.S. Dargusch, Promoting the columnar to equiaxed transition and grain refinement of titanium alloys during additive manufacturing, Acta Mater. 168 (2019) 261–274, https://doi.org/10.1016/j.actamat.2019.02.020.

[5] J.H. Rao, Y. Zhang, K. Zhang, A. Huang, C.H.J. Davies, X. Wu, Multiple precipitation pathways in an Al-7Si-0.6Mg alloy fabricated by selective laser melting, Scripta Mater. 160 (2019) 66–69, https://doi.org/10.1016/j.scriptamat.2018.09.045.

[6] J. Suryawanshi, K.G. Prashanth, S. Scudino, J. Eckert, O. Prakash, U. Ramamurty, Simultaneous enhancements of strength and toughness in an Al-12Si alloy synthesized using selective laser melting, Acta Mater. 115 (2016) 285–294, https://doi.org/10.1016/j.actamat.2016.06.009.

[7] A. Bin Anwar, Q.C. Pham, Selective laser melting of AlSi10Mg: effects of scan direction, part placement and inert gas flow velocity on tensile strength, J. Mater. Process. Technol. 240 (2017) 388–396, https://doi.org/10.1016/j.jmatprotec.2016.10.015.

[8] N.T. Aboulkhair, M. Simonelli, L. Parry, I. Ashcroft, C. Tuck, R. Hague, 3D printing of Aluminum alloys: additive Manufacturing of Aluminum alloys using selective laser melting, Prog. Mater. Sci. 106 (2019) 100578, https://doi.org/10.1016/j.pmatsci.2019.100578.

[9] K. Schmidtke, F. Palm, A. Hawkins, C. Emmelmann, Process and mechanical properties: applicability of a scandium modified Al-alloy for laser additive manufacturing, Phys. Procedia 12 (2011) 369–374, https://doi.org/10.1016/j.phpro.2011.03.047.

[10] M. Wang, R. Li, T. Yuan, C. Chen, L. Zhou, H. Chen, M. Zhang, S. Xie, Microstructures and mechanical property of AlMgScZrMn - a comparison between selective laser melting, spark plasma sintering and cast, Mater. Sci. Eng. 756 (2019) 354–364, https://doi.org/10.1016/j.msea.2019.04.060.

[11] A.B. Spierings, K. Dawson, T. Heeling, P.J. Uggowitzer, R. Schäublin, F. Palm, K. Wegener, Microstructural features of Sc- and Zr-modified Al-Mg alloys processed by selective laser melting, Mater. Des. 115 (2017) 52–63, https://doi.org/10.1016/j.matdes.2016.11.040.

[12] Y. Shi, K. Yang, S.K. Kairy, F. Palm, X. Wu, P.A. Rometsch, Effect of platform temperature on the porosity, microstructure and mechanical properties of an Al–Mg–Sc–Zr alloy fabricated by selective laser melting, Mater. Sci. Eng. A 732 (2018) 41–52, https://doi.org/10.1016/j.msea.2018.06.049.

[13] E.A. Marquis, D.N. Seidman, Nanoscale structural evolution of Al3Sc precipitates in Al(Sc) alloys, Acta Mater. 49 (2001) 1909–1919, https://doi.org/10.1016/S1359-6454(01)00116-1.

[14] R. Li, H. Chen, H. Zhu, M. Wang, C. Chen, T. Yuan, Effect of aging treatment on the microstructure and mechanical properties of Al-3.02Mg-0.2Sc-0.1Zr alloy printed by selective laser melting, Mater. Des. 168 (2019) 107668, https://doi.org/10.1016/j.matdes.2019.107668.

[15] A.B. Spierings, K. Dawson, P.J. Uggowitzer, K. Wegener, Influence of SLM scan-speed on microstructure, precipitation of Al3Sc particles and mechanical properties in Sc- and Zr-modified Al-Mg alloys, Mater. Des. 140 (2018) 134–143, https://doi.org/10.1016/j.matdes.2017.11.053.

[16] H. Zhang, D. Gu, J. Yang, D. Dai, T. Zhao, C. Hong, A. Gasser, R. Poprawe, Selective laser melting of rare earth element Sc modified aluminum alloy: thermodynamics of precipitation behavior and its influence on mechanical properties, Addit. Manuf. 23 (2018) 1–12, https://doi.org/10.1016/j.addma.2018.07.002.

[17] D. Ramos, F. Belblidia, J. Sienz, New scanning strategy to reduce warpage in additive manufacturing, Addit. Manuf. 28 (2019) 554–564, https://doi.org/10.1016/j.addma.2019.05.016.

[18] J. Suryawanshi, K.G. Prashanth, U. Ramamurty, Mechanical behavior of selective laser melted 316L stainless steel, Mater. Sci. Eng. A 696 (2017) 113–121.

[19] N. Nadammal, S. Cabeza, T. Mishurova, T. Thiede, A. Kromm, C. Seyfert, L. Farahbod, C. Haberland, J. Ann, P. Dolabella, G. Bruno, Effect of hatch length on the development of microstructure, texture and residual stresses in selective laser melted superalloy Inconel 718, Mater. Des. 134 (2017) 139–150, https://doi.org/10.1016/j.matdes.2017.08.049.

[20] Y. Lu, S. Wu, Y. Gan, T. Huang, C. Yang, L. Junjie, J. Lin, Study on the microstructure, mechanical property and residual stress of SLM Inconel-718 alloy manufactured by differing island scanning strategy, Optic Laser. Technol. 75 (2015) 197–206, https://doi.org/10.1016/j.optlastec.2015.07.009.

[21] C. Chen, J. Yin, H. Zhu, Z. Xiao, L. Zhang, X. Zeng, Effect of overlap rate and pattern on residual stress in selective laser melting, Int. J. Mach. Tool Manufact. 145 (2019) 103433, https://doi.org/10.1016/j.ijmachtools.2019.103433.

[22] K.Q. Le, C. Tang, C.H. Wong, On the study of keyhole-mode melting in selective laser melting process, Int. J. Therm. Sci. 145 (2019) 105992, https://doi.org/10.1016/j.ijthermalsci.2019.105992.

[23] I. Dragomir, T. Unga, The contrast factors of dislocations in cubic crystals: the dislocation model of strain anisotropy in practice, J. Appl. Crystallogr. (1999) 992–1002, https://doi.org/10.1107/S0021889899009334.

[24] W. Woo, T. Ungar, Z. Feng, E. Kenik, B. Clausen, X-ray and neutron diffraction measurements of dislocation density and subgrain size in a friction-stir-welded aluminum alloy, Metall. Mater. Trans. A 41 (2010) 1210–1216, https://doi.org/10.1007/s11661-009-9963-5.

[25] S. Jiang, H. Wang, Y. Wu, X. Liu, H. Chen, M. Yao, B. Gault, D. Ponge, D. Raabe, A. Hirata, M. Chen, Y. Wang, Z. Lu, Ultrastrong steel via minimal lattice misfit and high-density nanoprecipitation, Nature 544 (2017) 460–464, https://doi.org/10.1038/nature22032.

[26] J. Aufrecht, A. Leineweber, J. Foct, E.J. Mittemeijer, The structure of nitrogen-supersaturated ferrite produced by ball milling, Philos. Mag. A 88 (2008) 1835–1855, https://doi.org/10.1080/14786430802322198.

[27] T. Ungár, A. Borbély, The effect of dislocation contrast on x-ray line broadening: a new approach to line profile analysis, Appl. Phys. Lett. 69 (1996) 3173–3175.

[28] C.E. Kril, R. Birringer, Estimating grain-size distributions in nanocrystalline materials from X-ray diffraction profile analysis, Philos. Mag. A 77 (1998) 621–640, https://doi.org/10.1080/01418619808224072.

[29] Z. Szklarska-Smialowska, Pitting corrosion of aluminum, Corrosion Sci. 41 (1999) 1743–1767, https://doi.org/10.1016/S0010-938X(99)00012-8.

[30] J. Jorcin, M.E. Orazem, P. Nadine, B. Tribollet, CPE analysis by local electrochemical impedance spectroscopy, Electrochim. Acta 51 (2006) 1473–1479, https://doi.org/10.1016/j.electacta.2005.02.128.

[31] B. Hirschorn, M.E. Orazem, B. Tribollet, V. Vivier, I. Frateur, M. Musiani, Determination of effective capacitance and film thickness from constant-phase-element parameters, Electrochim. Acta 55 (2010) 6218–6227, https://doi.org/10.1016/j.electacta.2009.10.065.

[32] L. Parry, I.A. Ashcroft, R.D. Wildman, Understanding the effect of laser scan strategy on residual stress in selective laser melting through thermo-mechanical simulation, Addit. Manuf. 12 (2016) 1–15.

[33] H. Ali, H. Ghadbeigi, K. Mumtaz, Effect of scanning strategies on residual stress and mechanical properties of Selective Laser Melted Ti6Al4V, Mater. Sci. Eng. A 712 (2018) 175–187, https://doi.org/10.1016/j.msea.2017.11.103.

[34] D. Gu, Y.C. Hagedorn, W. Meiners, G. Meng, R.J.S. Batista, K. Wissenbach, R. Poprawe, Densification behavior, microstructure evolution, and wear performance of selective laser melting processed commercially pure titanium, Acta Mater. 60 (2012) 3849–3860, https://doi.org/10.1016/j.actamat.2012.04.006.

[35] C.B. Fuller, D.N. Seidman, D.C. Dunand, Mechanical properties of Al(Sc,Zr) alloys at ambient and elevated temperatures, Acta Mater. 51 (2003) 4803–4814, https://doi.org/10.1016/S1359-6454(03)00320-3.

[36] Y. Buranova, V. Kulitskiy, M. Peterlechner, A. Mogucheva, R. Kaibyshev, S. V. Divinski, G. Wilde, Al3(Sc,Zr)-based precipitates in Al–Mg alloy: effect of severe deformation, Acta Mater. 124 (2017) 210–224, https://doi.org/10.1016/j.actamat.2016.10.064.

[37] J. Kruth, M. Badrossamay, E. Yasa, J. Deckers, L. Thijs, J. Van Humbeeck, Part and material properties in selective laser melting of metals, 16th International Symposium on Electromachining.

[38] B. Cheng, S. Shrestha, K. Chou, Stress and deformation evaluations of scanning strategy effect in selective laser melting, Addit. Manuf. 12 (2016) 240–251, https://doi.org/10.1016/j.addma.2016.05.007.

[39] T. Rubben, R.I. Revilla, I. De Graeve, Influence of heat treatments on the corrosion mechanism of additive manufactured AlSi10Mg, Corrosion Sci. 147 (2019) 406–415, https://doi.org/10.1016/j.corsci.2018.11.038.

[40] P. Fathi, M. Mohammadi, X. Duan, A.M. Nasiri, A comparative study on corrosion and microstructure of direct metal laser sintered AlSi10Mg _ 200C and die cast A360. 1 aluminum, J. Mater. Process. Technol. 259 (2018) 1–14.

[41] H. Zhang, D.D. Gu, D.H. Dai, C.L. Ma, Y.X. Li, M.Z. Cao, S.H. Li, Influence of heat treatment on corrosion behavior of rare earth element Sc modified Al-Mg alloy processed by selective laser melting, Appl. Surf. Sci. 509 (2020) 145330.